



HAL
open science

Calibration of imaging plates to electrons between 40 and 180 MeV

N. Rabhi, K. Bohacek, D. Batani, G. Boutoux, J.-E. Ducret, E. Guillaume, K.
Jakubowska, C. Thauray, I. Thfoin

► **To cite this version:**

N. Rabhi, K. Bohacek, D. Batani, G. Boutoux, J.-E. Ducret, et al.. Calibration of imaging plates to electrons between 40 and 180 MeV. *Review of Scientific Instruments*, 2016, 87 (5), pp.103 - 103. 10.1063/1.4950860 . hal-01342482

HAL Id: hal-01342482

<https://hal.science/hal-01342482>

Submitted on 6 Nov 2019

HAL is a multi-disciplinary open access archive for the deposit and dissemination of scientific research documents, whether they are published or not. The documents may come from teaching and research institutions in France or abroad, or from public or private research centers.

L'archive ouverte pluridisciplinaire **HAL**, est destinée au dépôt et à la diffusion de documents scientifiques de niveau recherche, publiés ou non, émanant des établissements d'enseignement et de recherche français ou étrangers, des laboratoires publics ou privés.

Calibration of imaging plates to electrons between 40 and 180 MeV

N. Rabhi, K. Bohacek, D. Batani, G. Boutoux, J.-E. Ducret, E. Guillaume, K. Jakubowska, C. Thaury, and I. Thfoin

Citation: *Review of Scientific Instruments* **87**, 053306 (2016); doi: 10.1063/1.4950860

View online: <http://dx.doi.org/10.1063/1.4950860>

View Table of Contents: <http://aip.scitation.org/toc/rsi/87/5>

Published by the [American Institute of Physics](#)

Articles you may be interested in

[Validation of modelled imaging plates sensitivity to 1-100 keV x-rays and spatial resolution characterisation for diagnostics for the "PETawatt Aquitaine Laser"](#)

Review of Scientific Instruments **87**, 043108 (2016); 10.1063/1.4944863

[Study of imaging plate detector sensitivity to 5-18 MeV electrons](#)

Review of Scientific Instruments **86**, 113304 (2015); 10.1063/1.4936141

[Response functions of imaging plates to photons, electrons and \$^4\text{He}\$ particles](#)

Review of Scientific Instruments **84**, 103510 (2013); 10.1063/1.4826084

[Calibration of imaging plate for high energy electron spectrometer](#)

Review of Scientific Instruments **76**, 013507 (2004); 10.1063/1.1824371

[Absolute calibration for a broad range single shot electron spectrometer](#)

Review of Scientific Instruments **77**, 103301 (2006); 10.1063/1.2360988

[Calibration and equivalency analysis of image plate scanners](#)

Review of Scientific Instruments **85**, 11E604 (2014); 10.1063/1.4886390



Calibration of imaging plates to electrons between 40 and 180 MeV

N. Rabhi,^{1,a)} K. Bohacek,² D. Batani,¹ G. Boutoux,¹ J.-E. Ducret,¹ E. Guillaume,³
 K. Jakubowska,^{4,1} C. Thauray,³ and I. Thfoin⁵

¹CELIA (Centre Lasers Intenses et Applications), Université Bordeaux, CNRS, CEA, UMR 5107,
 F-33405 Talence, France

²ELI Beamlines, Institute of Physics ASCR, Prague, Czech Republic

³LOA, ENSTA ParisTech, École Polytechnique, Université Paris-Saclay, CNRS, 91762 Palaiseau, France

⁴Institute of Plasma Physics and Laser Microfusion, Hery Street 23, 01-497 Warsaw, Poland

⁵CEA DAM DIF, F-91297 Arpajon, France

(Received 1 December 2015; accepted 4 May 2016; published online 24 May 2016)

This paper presents the response calibration of Imaging Plates (IPs) for electrons in the 40-180 MeV range using laser-accelerated electrons at Laboratoire d'Optique Appliquée (LOA), Palaiseau, France. In the calibration process, the energy spectrum and charge of electron beams are measured by an independent system composed of a magnetic spectrometer and a Lanex scintillator screen used as a calibrated reference detector. It is possible to insert IPs of different types or stacks of IPs in this spectrometer in order to detect dispersed electrons simultaneously. The response values are inferred from the signal on the IPs, due to an appropriate charge calibration of the reference detector. The effect of thin layers of tungsten in front and/or behind IPs is studied in detail. GEANT4 simulations are used in order to analyze our measurements. *Published by AIP Publishing*. [<http://dx.doi.org/10.1063/1.4950860>]

I. INTRODUCTION

Petawatt lasers have been developed for state of the art research purposes, e.g., inertial confinement fusion, particle acceleration, and secondary particle generation sources (electrons, protons, ions, neutrons, etc.). These lasers can be combined with other large scale research facilities, such as charged particle accelerators, X-ray sources, and megajoule class lasers.¹

High energy particle beams produced by the interaction of the petawatt laser with solid target are continuously distributed in the energy up to few hundreds of MeV. Therefore, diagnostics capable of measuring and characterizing the high flux in a large energy range are necessary.

This article is dedicated to improve our knowledge of the response function of Imaging Plates (IPs) and sets of IPs to electrons in the energy range from 40 to 180 MeV. Monte Carlo simulations are used to analyze our measurements and permit to predict detector response functions up to 1 GeV.

This work is conducted in the framework of the PETawatt Aquitaine Laser (PETAL+) project. Our results will be anyhow useful for a large community, e.g., in laser plasma experiments or in electron imaging and microscopy.

The PETAL+ project^{2,3} aims at building the first diagnostics for PETawatt Aquitaine Laser (PETAL)⁴ on the Laser MégaJoule (LMJ) facility. These include an X-ray photon spectrometer for the 5-100 keV range and a set of charged-particle diagnostics:

(1) An energy spectrum measurement of charged particles accelerated from the PETAL laser target, so-called Spectromètre Électrons Protons A Grande Énergie (SEPAGE), (2)

a radiography detector for backlighting experiments of the LMJ targets, and (3) a set of two magnetic spectrometers to measure the electron energy spectra and their angular distribution around the axis of PETAL called Spectromètre ÉlectronS À Moyenne Énergie (SESAME).

The SESAME spectrometers will be placed on the chamber wall of LMJ. They are made of permanent dipole magnets, deflecting electrons, and protons with energies above 5 MeV. IP detectors are covering the magnet exit. They will be installed at 0° and 45° with respect to the PETAL laser axis.

The SEPAGE diagnostics is going to be positioned inside the LMJ chamber using a dedicated, so-called System for Insertion of Diagnostics. This diagnostic system will be placed on the normal to the PETAL target and is composed of two detection channels equipped with Thomson parabolas:⁵ a channel for “low-energy” charged particles (electrons, protons, and ions) in the range above 0.1 MeV, and a channel for “high-energy” charged particles, for particles above 8 MeV (see Fig. 1).

Detectors such as IP are sensitive to all kinds of ionizing particles and suitable to laser accelerated particle beams. The use of IP and sets of IP protected by high Z material (e.g., tungsten) instead of only single IPs for the detection of charged particles accelerated in the PETAL target is necessary because of the following points:

- (1) The system must be shielded against the X-ray background produced by laser-target interaction and material activation inside the LMJ interaction chamber.
- (2) The response of the system must be homogeneous over its entire surface, which is not obvious to achieve due to the mechanical structures of SESAME and SEPAGE, inside which the detectors are tightly fixed, and also due to the large dimensions, these detectors need to have in order to cover the energy spectra of both electrons and

^{a)}Author to whom correspondence should be addressed. Electronic mail: nesrine.rabhi@celia.u-bordeaux.fr

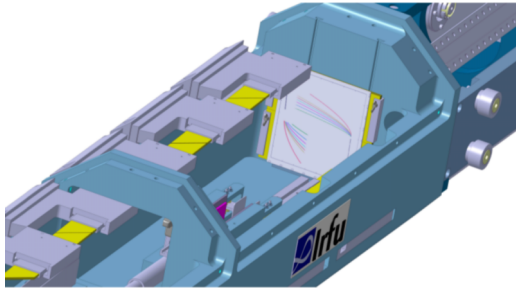


FIG. 1. The detection area of SEPAGE.⁶ The lateral electron detectors are shown in yellow color. The detector for high energy electrons (on the upper side) is 100 cm long, and the detector for low energy electrons (on the lower side) is 40 cm long. The front detectors for protons, ions, and electrons are shielded by 5 mm of tungsten placed behind.

ions. As it is observed in simulations and experiments,¹³ backscattering from material behind the IPs might lead to the increase of the signal depending on the particle type and energy as well as on the material itself. Therefore the response of the detectors must be made independent of the IP position inside SEPAGE.

II. IMAGING PLATES

Imaging plates (IPs) are 2-dimension passive detectors with roughly 500 μm thickness, composed of thin layers with various thicknesses and different compositions of the active (phosphoric) layer.^{7,8} There are 5 types of IPs named BAS-MS, BAS-SR, BAS-TR, BAS-MP, and BAS-ND produced by the Fuji company. The compositions of MS, SR, and TR IP are given in Table I (as described in Ref. 7). The compositions of BAS-MP and BAS-ND are unknown to us, and hence we did not use them in our study.

The advantages of IPs are their light weight, re-usability, high efficiency to various types of particles in a large energy range as well as their large dynamic range, above 10^8 .⁸

Every type of IP has a phosphoric layer. A part of the energy deposited in this phosphor layer by ionizing particles generates metastable states of Eu^{3+} ions and FI^- or FBr^- centers. Electrons trapped in these states can be released and can recombine to the initial molecular states. This phenomenon is triggered by photons and results in the emission of 3 eV photons, which are called Photostimulated Luminescence (PSL) and are recorded by a scanner at the readout time. The IP response function is the average number of PSL per incident ionizing particle. It is a function of the type of particle (charge, mass, and kinetic energy) and of the type of IP. It is closely related, as described below, to the average particle energy loss within the phosphoric layer of the IP. It is of crucial importance to determine experimentally this response in order to be able to reconstruct the absolute number of particles passing through an IP once the type of these particles and their energies are known.

To our knowledge, there is no available data on the response function of Fuji MS and TR IPs for electrons with energy above 20 MeV, where published data of Fuji SR IP⁹⁻¹³ are also scarce. In 2005, Tanaka *et al.*⁹ measured the response of SR IP with 11.5, 30, and 100 MeV using a BAS-1800 scanner. In 2008, Nakanii *et al.*¹⁰ measured the SR IP response to 1 GeV electrons. Chen *et al.*¹¹ worked with the same type of IP from 100 keV to 4 MeV using a FLA-7000 scanner. In 2013, Bonnet *et al.*⁷ measured the response of three types of IP in the energy range between 0.6 and 3.2 MeV for protons. Their study permitted to estimate the responses of IPs to other types of particles such as photons, electrons, and ^4He .¹² In our experiment on ELSA at Bruyères-le-Châtel,¹³ we used 5, 10, and 18 MeV mono-energetic electrons. This work shows basic agreement with the literature.

The Particle-In-Cell (PIC) simulations performed for the PETAL laser¹⁴ show that electron and proton energy spectra will extend above 100 MeV. It is therefore necessary to perform the calibration of IPs in this energy range. This is the purpose of the present work.

TABLE I. Atomic compositions, densities, and thicknesses of the layers of SR, MS, and TR IP.

Layer	SR	MS	TR
PROTECTIVE			
Composition	$\text{C}_2\text{H}_2\text{O}$	$\text{C}_2\text{H}_2\text{O}$	No layer
Density (g/cm^3)	1.273	1.66	0
Thickness (μm)	6	9	0
SENSITIVE			
Composition	BaFBr:Eu	BaFBr _{0.85} I _{0.15} :Eu	BaFBr _{0.85} I _{0.15} :Eu
Density (g/cm^3)	3.1	3.31	2.85
Thickness (μm)	120	115	50
SUPPORT			
Composition	$\text{C}_2\text{H}_2\text{O}$		
Density (g/cm^3)	1.273	1.66	1.66
Thickness (μm)	188	190	250
MAGNETIC			
Composition	$\text{ZnMn}_2\text{Fe}_5\text{NO}_{40}\text{H}_{15}\text{C}_{10}$		
Density (g/cm^3)	3.1	2.77	2.77
Thickness (μm)	160	160	160

To read the IPs after the irradiation, we use a FLA-7000 scanner with the resolution of $50 \mu\text{m}$, sensitivity 4000 and latitude 5.

III. EXPERIMENTAL SETUP

The laser-plasma electron accelerator from the ‘‘Salle Jaune’’ facility at LOA is used as the high energy electron source. The laser system provides pulses with a duration of 30 fs, a maximum energy of 2 J after compression, a central wavelength of 800 nm and operates at the maximum repetition rate of 1 Hz.

The acceleration is achieved by the interaction of this 60 TW laser pulse with an underdense plasma in the relativistic regime. This plasma is created by the laser pulse itself from a helium gas target. The accelerator generates electron bunches with energies up to a few hundreds MeV, divergence below 5 mrad, charge (up to 100 pC) and electron bunch duration in tens of femtoseconds.¹⁵ The reason to choose this facility was the similarity of the provided electron bunches in total charge and time structure comparable with those that will be generated by the PETAL laser.

The accelerated electrons are analyzed by a magnetic spectrometer placed outside of the vacuum chamber. The distance between the gas jet used as the electron source and the front of the spectrometer magnet is $D_{JM} = 800 \text{ mm}$. Electrons pass through a 1 cm thick glass window of the vacuum chamber before entering the spectrometer. The average energy loss of the electrons is small (a few MeV). It was not considered in our experiment since the electron beams are characterized by the magnetic spectrometer downstream of this vacuum window. The electrons are entering the magnet gap perpendicularly (see Fig. 2) to its entrance surface.

The magnetic system is composed of two plane dipole magnets. Electrons are passing between the magnets through the gap of width $l_{mag} = 100 \text{ mm}$ and height $h_{mag} = 10 \text{ mm}$. The magnetic length of the dipole is $L_{mag} = 100 \text{ mm}$. The dipole magnetic field in this gap is equal to $B = 1.1 \text{ T}$ and the measured magnetic field outside the magnet gap is equal to zero. The edge field region is small enough and does not significantly alter electron trajectories when compared to the simplified magnetic field step-like structure. For a magnetic field of this kind, it is possible to derive analytical formulas for electron trajectories through the whole setup. A Lanex screen is used as a standard electron detector.

The advantage of this setup is the possibility to insert IPs between the magnet and Lanex screen with a small

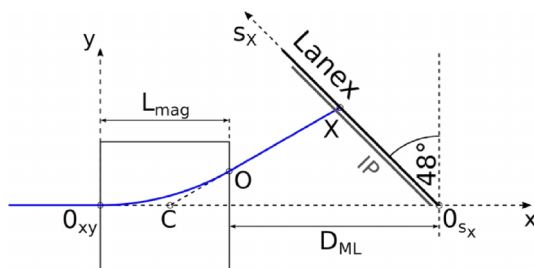


FIG. 2. Sketch of the spectrometer and definition of the geometrical parameters.

perturbation of the measurement in this energy range on the Lanex screen as well as on our detectors. Our GEANT4¹⁶ simulations detailed below show that in the energy range covered by our experiment, the electron tracks are hardly affected by our thin detectors and that the Lanex screen is far enough from our detectors not to influence them. In our experiment, the Lanex screen is used as the reference detector to reconstruct the number of electrons incident on the IPs.

Electrons accelerated by the laser pulse are recorded simultaneously on an IP and on the Lanex screen behind it, as shown in Fig. 3. It should be emphasized that, as can be seen in Fig. 3, the images on IP and on the Lanex screen can be superimposed giving the same information in both.

The Lanex screen contains a phosphoric layer which emits light in the visible range (around 546 nm) when an electron passes through. It can be assumed that the emitted light is proportional to the energy deposited in this layer by the particles. For electron energies above 1 MeV, the energy deposited in the phosphoric layer of the Lanex screen becomes independent of the incident electron energy.¹⁷

The fraction of the emitted photons, which escape the back side of the Lanex screen, is then collected by the pixels of the Charge Coupled Device (CCD) camera equipped with a lens. In order to calibrate the response of our detectors as a function of the electron energy, an independent measurement of the electron energy spectrum corresponding to the signal measured is provided by magnetic spectrometer, whose geometry is described below.

$D_{ML} = 160 \text{ mm}$ is the distance between the exit from the magnet and the edge of the IP/Lanex detectors (see Fig. 2). The length of the Lanex screen in the dispersive dimension of the system is $L_{Lanex} = 170 \text{ mm}$ and the angle of the Lanex screen $\theta_{Lanex} = 48^\circ$ with respect to the direction orthogonal to the laser axis.

We define a coordinate system (x, y) with the origin $O_{xy} = (0, 0)$ at the intersection of the electron trajectory with the front edge of the magnet and with the x -axis following the laser axis (see Fig. 2). We can write for the coordinates of electrons at the magnet exit plane,

$$\begin{pmatrix} x_O \\ y_O \end{pmatrix} = \begin{pmatrix} L_{mag} \\ R - \sqrt{R^2 - L_{mag}^2} \end{pmatrix}, \quad (1)$$

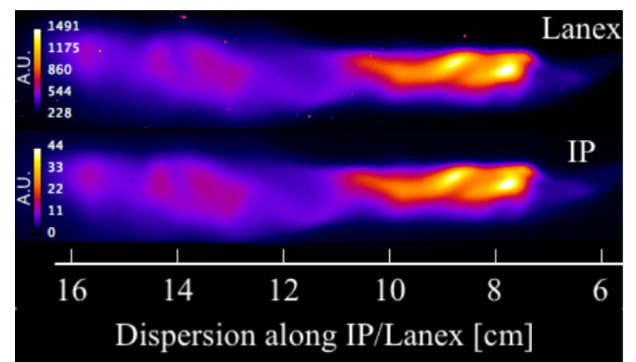


FIG. 3. Comparison of the recorded signal (here in arbitrary units) on the Lanex screen (top) and on the IP (bottom).

where R is the radius of the electron trajectory in the constant magnetic field B ,

$$R = \frac{\beta\gamma m_e c}{eB}. \quad (2)$$

In this formula, $\beta = v/c$ is the velocity of the electron, γ is the relativistic Lorentz factor, m_e is the electron mass, c is the speed of light, and e is the electron charge.

The coordinates of point C , which is the intersection of two straight electron trajectories before entering and after exiting the magnet, can be written as

$$\begin{pmatrix} x_C \\ y_C \end{pmatrix} = \begin{pmatrix} (x_O^2 + y_O^2)/(2x_O) \\ 0 \end{pmatrix}. \quad (3)$$

The next point to consider is the intersection of the straight electron trajectory after exiting the magnet and the Lanex screen. Coordinates of this point can be written as

$$\begin{pmatrix} x_X \\ y_X \end{pmatrix} = \begin{pmatrix} L_{mag} + D_{ML} - y_X \tan(\theta_{Lanex}) \\ \frac{y_O(L_{mag} + D_{ML} - x_C)}{x_O - x_C + y_O \tan(\theta_{Lanex})} \end{pmatrix}. \quad (4)$$

We also introduce the dispersion defined as $s_X = y_X/\cos(\theta_{Lanex})$, which is the distance from the laser axis (with the origin 0_{s_X}) along the Lanex screen. The dispersion curve $s_X = f(E)$ obtained using the parameters given above is shown in Fig. 4.

The above formulas do not take into account the divergence of the electron beam. The beam divergence convoluted with multiple scattering inside the vacuum window leads to a dispersion on the detectors which can be estimated with the non-dispersive coordinate (vertical in Fig. 3). This dispersion is roughly constant as function of the electron energy with a value of $y \sim 7$ mm (FWHM). The spatial dispersion generates an uncertainty on the relationship between the dispersive coordinate and the actual electron energy given by

$$\delta E = \frac{\delta y}{ds/dE}. \quad (5)$$

This uncertainty is taken into account in the presentation of the results below.

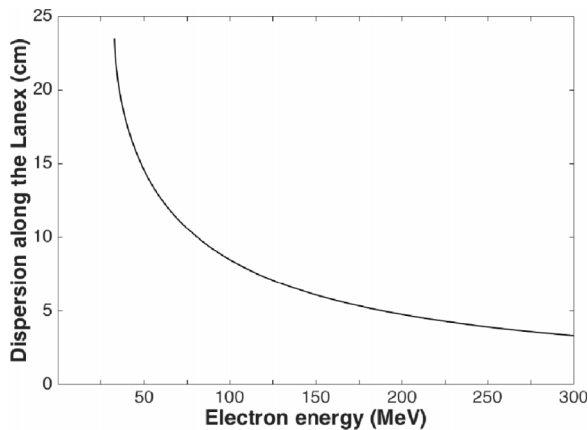


FIG. 4. The dispersion along the Lanex screen with respect to the electron energy.

IV. ELECTRON SPECTRUM MEASUREMENT

The measurement of spectrum and charge using the Lanex screen requires detailed knowledge of its parameters. Most of them were measured and described in Ref. 17 and were the same during our experiment. They are briefly described below.

The scintillator layer of Kodak Lanex Fine contains molecules of $Gd_2O_2S:Tb$ with the density $\rho_{Lanex} = 7.44$ g/cm³ and with the phosphoric surface loading $h_S = 0.033$ g/cm².

The number of photons N_{cr} created in the phosphoric layer of the Lanex screen at the central wavelength per incident electron can be calculated as

$$\frac{dN_{cr}}{dN_{el}} = \frac{1}{E_{ph}} \varepsilon \frac{dE}{dx} \delta x, \quad (6)$$

where dE/dx is the stopping power, ε is the fraction of the energy loss converted into phosphoric photons, $E_{ph} = 2.27$ eV is the energy of photon with the wavelength of 546 nm (other wavelengths will be absorbed within an interference filter in front of the CCD camera), and $\varepsilon dE/dx = 1.8 \pm 0.2$ MeV/cm is the yield of electron kinetic energy that is transformed into visible light. Note that for energies above 1 MeV (as is stated in part III), this yield is independent of the electron energy. Moreover, $\delta x = h_S/\rho_{Lanex} \cos(\theta_{perp})$ is the equivalent thickness of gadolinium oxysulfide, where $\theta_{perp} = \theta_{Lanex} - \theta_e$ is the angle between the normal to the Lanex screen and the electron trajectory, and $\theta_e = \text{atan}(y_X/(x_X - x_C))$ is the angle of the electron trajectory relative to the x-axis.

The number of photons collected by the CCD camera per one photon created in the Lanex screen is given by the formula

$$\frac{dN_{coll}}{dN_{cr}} = \zeta g(\theta_{CCD}) q_l q_w q_f q_m \delta \Omega, \quad (7)$$

where $\zeta = 22\%$ is the transmission output factor of photons (i.e., the fraction of photons that escape the Lanex screen), $g(\theta_{CCD}) = \cos(\theta_{CCD})/\pi$ is the angular distribution of photons escaping the Lanex screen,¹⁸ $q_l = 0.95$, $q_w = 0.95$, and $q_f = 0.36$ are transmission factors of the camera lens, the camera window, and the interference filter, respectively, $q_m = 0.97$ is the reflection coefficient of the silver mirror between the CCD and the Lanex screen, and $\delta \Omega = 0.002$ sr is the solid angle of collection (given by the area of the camera lens and the distance of the lens from the Lanex screen).

A 16-bit CCD camera Andor DV-420 is used for detection. This camera has a quantum efficiency $QE = 26.5\%$ at 546 nm and -20°C , and $r = 7$ electrons are needed to create one count. The CCD yield is therefore

$$\frac{dN_{cts}}{dN_{coll}} = \frac{QE}{r}. \quad (8)$$

The formulas above allow to derive the relationship between the CCD signal and the number of electrons on the Lanex screen,

$$\frac{dN_{el}}{dE}(E_0) = \frac{Cts(E_0)}{\delta s_{pix}} \frac{ds_X}{dE} \div \left(\frac{dN_{cr}}{dN_{el}} \frac{dN_{coll}}{dN_{cr}} \frac{dN_{cts}}{dN_{coll}} \right), \quad (9)$$

where $Cts(E_0)$ is the number of CCD counts for a given energy E_0 (obtained by integrating pixel counts in the non-dispersive dimension over the divergence of 24 mrad) and

$\delta s_{pix} = 0.257$ mm is the pixel size projected on the Lanex screen.

The camera was imaging the Lanex screen by the reflection from a silver mirror to prevent altering the signal by incoming electrons. This mirror has the reflection coefficient of 97% for 3 eV photons which has to be taken into account in the electron charge calculations.

The signal of the camera could, however, be affected by secondary X-rays produced in the interaction of electrons with the setup. For this reason, a shielding made of two lead bricks of 11 cm thickness was used. Some X-rays could still reach the camera during every exposure but their number is generally much lower than the signal created by electrons in the Lanex screen. Moreover, the signal from the X-rays can be removed using the background subtraction and “median filtering” of an 4×4 px area around each pixel of the CCD camera. Therefore the influence of X-rays on the detected signal is negligible.

The different steps from the signal generation on the Lanex screen to its collection on the CCD contribute to the overall uncertainty in the electron charge determination. The transmission factors of the green bandpass filter and the camera lens were measured with a precision better than 1%. We do not have any information about the uncertainties in the measurements of the transmission factors of the interference filter, of the lens, and of the window used for the characterization done by Glinec *et al.*¹⁷ There is also an uncertainty of 1% in the photon collection by the CCD. If we consider the same uncertainty in the photon collection during our experiment, we obtain an error of 3% from the quantified uncertainties.

The whole detection system of the Lanex screen + CCD was calibrated at the ELYSE facility¹⁹ with 9 MeV electrons produced in bunches of up to 5 nC and with Integrating Current Transformers¹⁷ (ICTs). The estimated uncertainty on the absolute number of electrons given by the ICT was determined at the 50% range in Ref. 17, therefore dominating the uncertainty of our Lanex reference detector. However, such an absolute uncertainty with the same type of screens was estimated to be in the 10% range in Ref. 20. We have included below a discussion on the errors of our measurements which shows that our errors are between these two values.

Using Eq. (9) and all parameters mentioned above, the spectrometer system is absolutely calibrated and we can obtain electron spectra (the number of electrons per MeV with respect to the energy) for the laser-plasma electron accelerator. A measured electron spectrum is shown in Fig. 5. The electron energy spectrum obtained after deconvolution of the Lanex screen signal with dispersion curve (Fig. 4) is shown in Fig. 6. The amplitude of the spectrum was found using the parameters mentioned above.

V. CHARGE CALCULATION AND ENERGY DEPENDENCE

The number of detected electrons can be obtained by integrating the formula (Eq. (9)) with respect to the energy. We divide the Lanex screen and the IP into energy intervals

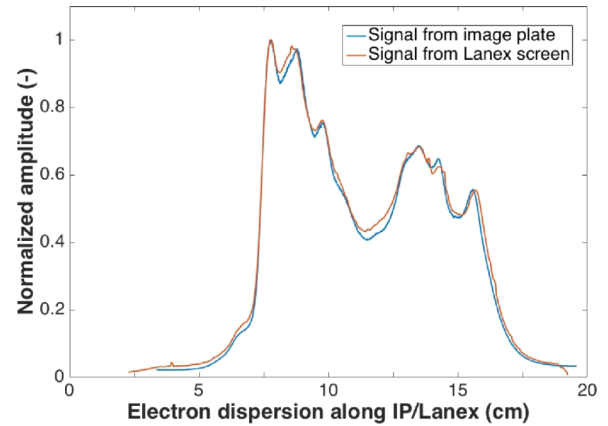


FIG. 5. The comparison of the signal profile obtained from an imaging plate (blue) and the signal profile detected by the Lanex screen (red). The amplitude of the uncalibrated profiles are normalized to unity in order to compare the shape of the profiles.

of 10 MeV in order to compare the signal for specific parts of energy spectrum using the dispersion relationship of Fig. 4.

The comparison of the IP and Lanex signals allows an absolute positioning of the IP with respect to the Lanex screen and to the magnet transport. This permits the calculation of the electron energy spectrum on the IP. The IP response in PSL/ e^- can then be determined for each energy interval.

VI. RESPONSES OF IMAGING PLATES

A. Experimental results

The determined responses using electron energy between 40 and 180 MeV for MS, SR, and TR IP are shown in Fig. 7. The PSL per electron values for each type of IP are corrected for the effective thickness variation as a function of the position on the detector. Indeed, it has to be taken into account that electrons were passing through IP under various and non-zero angles with respect to the detector normal based on their energy (from -8° for $E = 40$ MeV to 37° for $E = 180$ MeV). Therefore, we introduce a multiplication factor $\cos(\theta_{\text{perp}})$ to

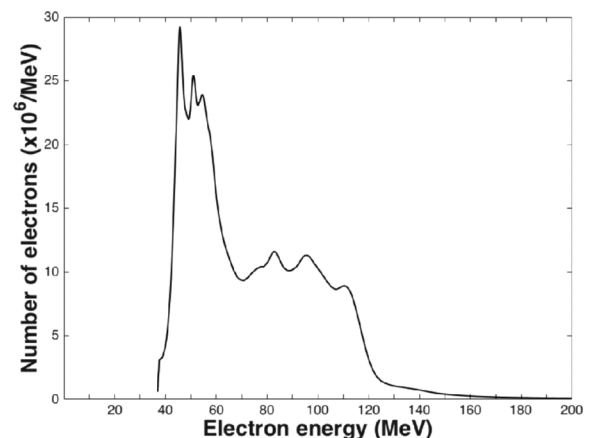


FIG. 6. The electron spectrum obtained from the Figure 5 deconvolved of the Lanex screen signal with the dispersion function. The amplitude of the spectra was found using the parameters mentioned above.

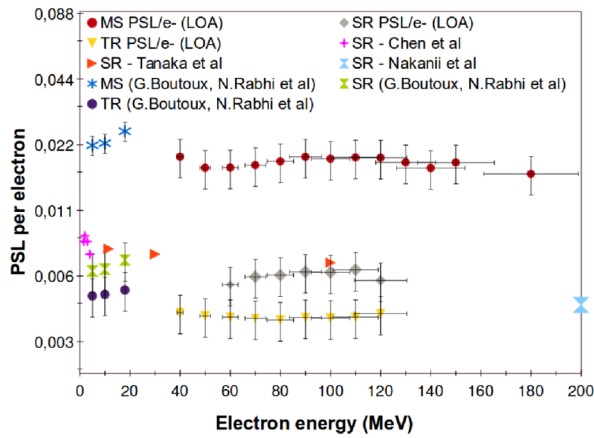


FIG. 7. The results of PSL per electron for the MS, SR, and TR IP. Notice that Nakanii data point was measured at 1 GeV.

normalize the IP signal properly to the electron trajectory normal to the IP detector.

The PSL/e^- responses for each type of IP are corrected for the fading effect. The fading time in our experiment is 2 min with few seconds uncertainty. This corresponds to signal losses between 2%, 5%, and 15% for MS, SR, and TR, respectively. The uncertainty on the fading time dependence is 7%.¹³ Therefore, in our case the uncertainty coming from the fading correction is 7% of, respectively, 2%, 5%, and 15% and hence negligible with respect to the other uncertainties in the calibration.

Results for higher electron energies are presented for MS IP (above 120 MeV), for which there is sufficient signal for our analysis. Our response functions of MS, SR, and TR are comparable with our previous work¹³ with Tanaka *et al.*⁹ and Nakanii *et al.*¹⁰

The PSL/e^- values for each type of IP (see Fig. 7) are almost constant as the electron energy increases. In this energy range, the TR IPs are less sensitive, and the MS IPs are more sensitive due to the composition and thickness of the phosphoric sensitive layer.

Each measurement is repeated seven times. The relative error on the responses is calculated for each type of IP and in each energy range separately as the relative standard deviation. These errors are 5% (MS), 3% (TR), and 7% (SR), respectively. As explained below, our total error bar is roughly 20% and is shown in Fig. 7 and followings.

B. GEANT4 simulations and models of imaging plates

The simulation of the experimental results is done with GEANT4¹⁶ considering the geometry and atomic composition of IPs (which vary according to the IP types) and using various physics libraries to calculate the deposited energy in the sensitive layer. Note that we named the deposited energy in the sensitive layer “Edep” in the rest of this article.

GEANT4 permits to track particles inside a material and to provide information about their energy deposit and position with a chosen precision.

The total deposited energy in the sensitive layer comes from the ionization induced by the incident particle, from

secondary particles (mostly electrons) that are produced in the protective and the sensitive layers, and from photons of bremsstrahlung and fluorescence processes, which are produced in the IPs and which can lose energy in the sensitive layer by photoelectric effect or Compton scattering. In GEANT4, various physics libraries describe the interaction of particles with matter. These libraries differ in the type of the interaction phenomena of the particles with matter. The electromagnetic (EM) model used in our simulations extends the coverage of EM interactions of particles (electrons, photons, hadrons, and ions) with the matter to low energies. This library is composed of several libraries, like the PENELOPE model (PENetration and Energy LOSS of Positrons and Electrons), which gives a detailed description of the low energy physics like the atomic effect, and it treats the EM interactions of electrons and photons in the energy range between 250 eV and 1 GeV. Another model included in the EM library is EM_OPT3 which is designed for applications that require higher accuracy of tracking particles, which interact electromagnetically, without magnetic fields. EM_OPT1 is designed for the analysis of the Compact Muon Solenoid (CMS), TeV ranges, and specific detector materials and the predicted energy loss of the EM_OPT1 could differ up to a factor 2 with respect to other models, which is a reason not to use it. In Ref. 13, we did a detailed study of the influence of different GEANT4 libraries on the response function of the IPs. We concluded that to ensure the best reliability of our simulations, only simulations with the EM standard physics list and the PENELOPE library should be used. Using these libraries, we identified the different contributions to the energy loss, e.g., from primary electrons or from secondary particles.

The calculated average energy losses of the electrons in the active layer of different IPs vary at a few percent level when using various GEANT4 libraries in the energy range of our experiment 40-180 MeV. This is negligible with respect to the uncertainties on the absolute values of the IP responses we determined.

In order to calculate the response functions from the deposited particle energy, we used two models, from the work of Hidding *et al.*²¹ and from Bonnet *et al.*^{7,12} In the model of Hidding *et al.*, the response function $R(\text{PSL}/e^-)$ is proportional to the energy deposited in the active layer. The sensitivity of IP is represented by the parameter α which defines this proportionality,

$$R(\text{PSL}/E(e^-)) = \alpha E_{\text{dep}}. \quad (10)$$

Bonnet *et al.* modified this model by taking into account the depth dependence of the PSL photon collection efficiency and introduce the following expression for R :

$$R(\text{PSL})E(e^-) = \alpha \int_0^w \frac{dE_p}{dz} \times \exp\left(\frac{-z}{L}\right) dz. \quad (11)$$

In this equation, z is the depth in the phosphoric film of thickness W , L is the absorption length of the PSL photons, and dE_p/dz is the deposited energy profile.

The energy loss profile in the active layer of an MS IP computed with GEANT4 is shown in Fig. 8 for 30 and 100 MeV electrons. We see that for both energies, the

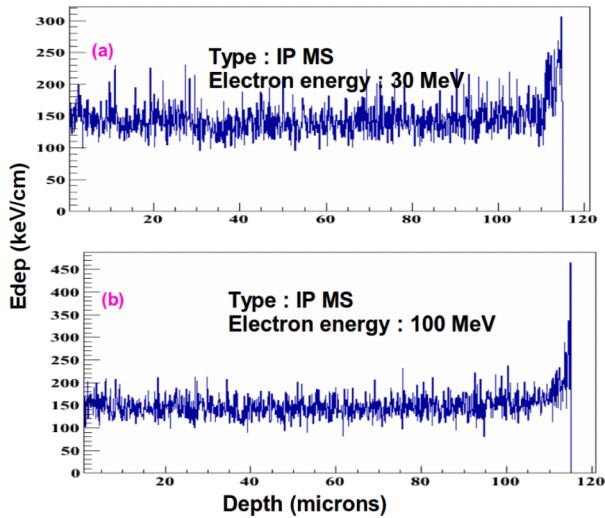


FIG. 8. The deposited energy in function of the depth of the IP MS with GEANT4 simulation. (a) An IP MS using electrons 30 MeV; (b) an IP MS using electrons 100 MeV.

stopping power is constant inside the layer except for the very last micrometers where an additional contribution of backscattering from the support layer can be seen.

In the following discussion, the given α values are computed with the Bonnet model using the absorption lengths for each type of IP. We have integrated numerically Eq. (11) on the energy loss profile computed for each electron energy. The sensitivities α are determined as the mean of the seven measurements performed with each type of IP. They are given in Table II and show a good agreement with Ref. 13.

Fig. 9 shows the PSL/e⁻ response for the IPs in the energy range between 0.1 and 1000 MeV using both models. We can see from this figure that the simulation provides a fair description of the data points in the energy range where data exist for electrons.

VII. ERROR ESTIMATION

We have discussed above the contributions of different parts of the Lanex screen reference detector and read-out to the uncertainty in the absolute number of electrons impinging on our detectors. Following Ref. 17, it seems that this uncertainty is dominated by the calibration of the Lanex detector and is given at the 50% level, which is in contradiction with Ref. 20, where this uncertainty is given at the 10% level.

In order to estimate the normalization of our data, we have compared them with the responses we obtained at

TABLE II. α values obtained with Bonnet *et al.* model¹² and comparison with the literature.

α in (10^{-4})	Boutoux, Rabhi <i>et al.</i> ¹³		
	Our results (EM-OPT4 physics library)	(EM-OPT4 physics library)	Bonnet <i>et al.</i> ¹²
α_{MS}	5.0 ± 1.1	6.8 ± 1.3	6.95 ± 1.6
α_{SR}	1.9 ± 1.3	2.2 ± 0.5	3.33 ± 0.8
α_{TR}	3.5 ± 0.8	4.7 ± 0.9	4.85 ± 1.35

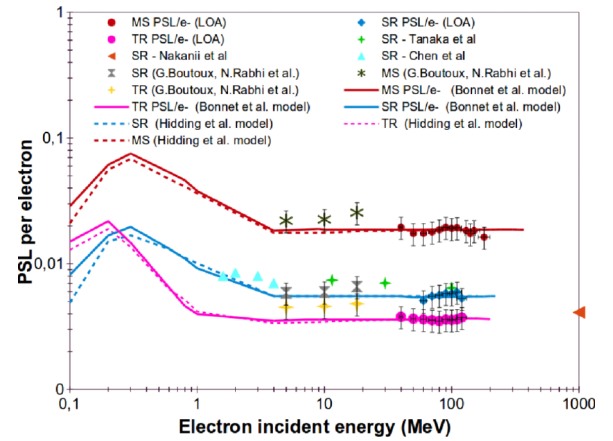


FIG. 9. The response of IPs with respect to the incident electron energy.

ELSA.¹³ To do so, we use the sensitivities obtained at ELSA within Bonnet's model and combine them with the GEANT4 calculation of the deposited energy of our experiment. We therefore make the assumption that the differences between both sets of data come from the variation of the energy loss profiles of the electrons in the IP, which should not be far from the truth, given that the responses are not very different.

The comparison between our data, averaged over the energy spectra and the different measurements and the values obtained with ELSA's sensitivities, is given in Table III for all three types of IP. We see from this table a clear agreement well within the error bars. Moreover, the RMS of the different measurements in our experiment is at the few percent level, in agreement with the estimated relative error of our experiment. From this table, we infer that the error bar on the absolute value of the responses we determine in the present experiment is compatible with that we obtained in our measurement at ELSA, i.e., at the 20% level.

VIII. IMAGING PLATE RESPONSES WITH TUNGSTEN PLATES

In SEPAGE and SESAME, the IPs used to detect particles will have to be shielded against high-energy photons. As mentioned above, IPs are detectors sensitive to all types of ionizing particles. Therefore, they are also sensitive to the large amount of high energy photons produced in the interaction of the laser with its target. As mentioned in the Introduction, IP to be used for charged particle detection at petawatt lasers has to be shielded particularly against photons above a few tens of keV (below this value there are sufficiently shielded by the mechanical structure of the diagnostics). To do so, the

TABLE III. Comparison between this work and estimates using IP sensitivities obtained by Ref. 13.

Type	$\alpha(\text{ELSA})^* \text{Edep}(\text{GEANT4}) (10^{-2})$	Mean (PSL/e ⁻) (10^{-2})	RMS (%)
MS	2.69 ± 0.54	1.85 ± 0.45	4
SR	0.68 ± 0.13	0.64 ± 0.15	4
TR	0.48 ± 0.1	0.37 ± 0.07	2.64

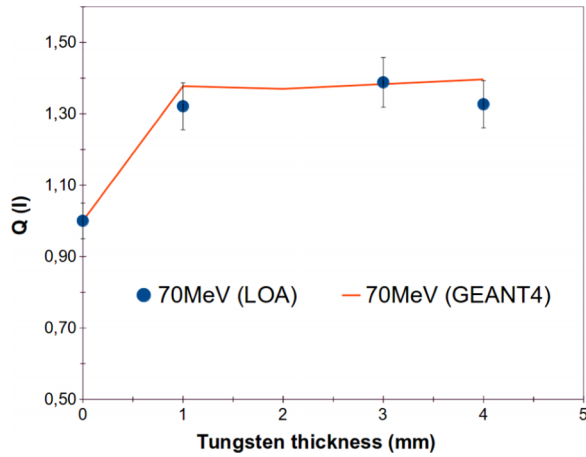


FIG. 10. The influence of tungsten behind the MS IP. The error bars show the relative error.

most efficient way is to use high-Z material such as tungsten. In this scope, we have performed measurements with IP with plates of tungsten in order to measure the influence of this high-Z material on the IP response. This is the goal of the present section to give the results and their comparison with the GEANT4 simulation.

We have measured IP responses with tungsten plates of various thicknesses (between 1 and 4 mm) placed behind and in front of the IP. For the purpose of comparison of the response function of IPs in the stacks $R(MS(I))$ to the response function of the same type of a single IP $R(MS(0))$, we introduce the ratio $Q(I)$ between these functions, measured with different laser shots,

$$Q(I) = R(MS(I))/R(MS(0)), \quad (12)$$

where I is the index of the measurement. The ratio is used in Figures 10, 12, and 13. By definition, $Q(I)$ is only sensitive on the relative uncertainty of the measurement, i.e., independent of the absolute efficiency of the reference detector.

As we can see from Fig. 10, the ratio $Q(I)$ increases when we add up to 4 mm of tungsten behind the IP. The signal increases when 1 mm of tungsten is added and remains constant when adding an extra thickness. We conclude therefore, at variance with our previous experiment¹³ which was performed at lower electron energy, that 1 mm of tungsten is sufficient to ensure signal independence with respect to

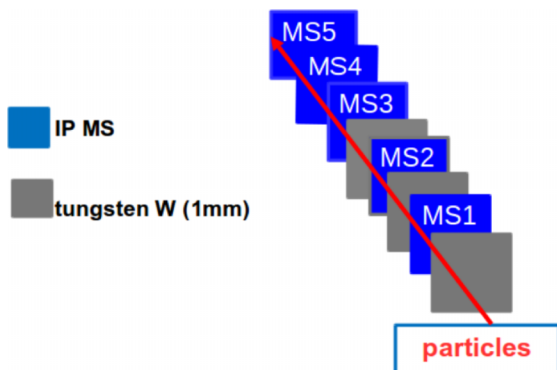


FIG. 11. The IP stack used in this work.

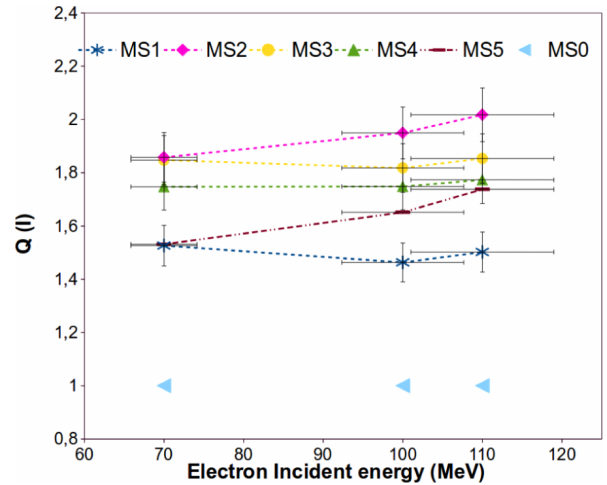


FIG. 12. The ratio $Q(I)$ for three electron energies. The dashed lines are guidelines.

material behind the IPs when installed inside the diagnostics (SESAME and SEPAGE). Moreover, we note that the response increases with the tungsten thickness, which means a higher detection efficiency, and that this increase is well described by our GEANT4 simulation.

We also tested a stack composed of tungsten plates (1 mm) and 5 MS IPs as shown in Fig. 11. We can see from Fig. 12 that the sensitivity of the IP MS(1) in the stack (the stars in dark blue color) is higher compared to a single IP MS(0) (the triangles in light blue color). The signal increases again for MS(2) (pink color) as compared to MS(1) in the stack. MS(3), MS(4), and MS(5) have equal or lower responses compared to MS(2).

The increase of the signal of the IPs in the stack showed in Fig. 12 compared to a single IP (MS(0)) is significantly larger than in the previous stack (Fig. 10). GEANT4 simulations are used to determine the physical origin of the signal increase on the IP. As it is shown in Figure 13, the additional amount of signal in the IP (the remaining difference between the full calculation and the explicitly identified contributions from primary and secondary electrons) comes from the

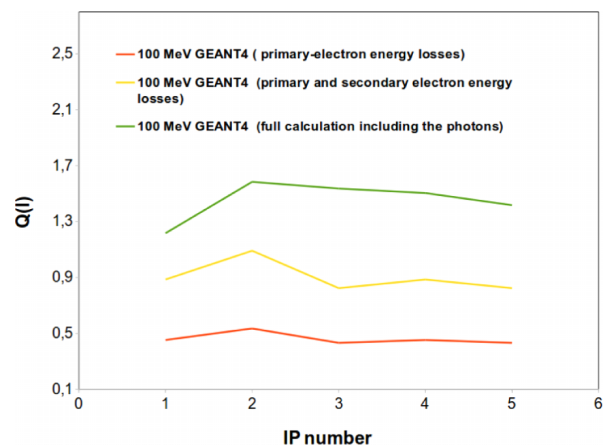


FIG. 13. The plot of $Q(I)$ (see text) with respect to the IP index in the stack of Fig. 12 (points). The solid lines show the calculation from GEANT4 simulations.

interaction of secondary photons with the IP active layer, which are either absorbed or producing tertiary ionization electrons.

IX. CONCLUSIONS

Using the laser-plasma electron source from the “Salle Jaune” facility at LOA, we have measured the IP responses for electrons in the range (40-180) MeV. We find almost constant responses and sensitivities for single IPs in agreement with previous studies. Our results are well explained by our detailed GEANT4 simulation of the interaction of the electrons with the IP materials.

We also show that the shielding material to be used for protecting IPs from the high-energy photons will not decrease the detection efficiency but rather increase it, whether it is placed in front of the IPs or behind them with respect to the electron trajectories. In particular, we showed that 1 mm of tungsten is sufficient to obtain IP responses independent from the material placed behind it with respect to the electron trajectories. We also observe that tungsten in front of the IP provides a higher increase of the IP sensitivity than tungsten installed behind. This will improve the efficiency to our detectors, which is important especially during, for example, the PETAL laser energy ramp up at the beginning of operations. These results are well explained with our GEANT4 simulation. Therefore, GEANT4 seems to be well qualified to design passive detectors for Petawatt laser accelerated charge particles. In particular, we will use it to design our electron detectors in PETAL+ and interpret future experiments using our GEANT4 simulation.

ACKNOWLEDGMENTS

This work is supported by the EQUIPEX PETAL+, Contract No. ANR-10-EQPX-0048, and partially supported by the Ministry of Education, Youth and Sports of the Czech Republic: ECOP3 (Grant No. CZ.1.07/2.3.00/20.0279), ELI Beamlines (Grant No. CZ.1.05/1.1.00/02.0061), and GA CR Grant No. 15-03118S.

- ¹C. Danson *et al.*, *High Power Laser Sci. Eng.* **3**, e3 (2015).
- ²D. Batani *et al.*, *Acta Politechnica* **53**, 103 (2013).
- ³J.-E. Ducret *et al.*, *Nucl. Instrum. Methods Phys. Res., Sect. A* **720**, 141 (2013).
- ⁴N. Blanchot *et al.*, *EPJ Web Conf.* **59**, 07001 (2013).
- ⁵J. J. Thomson, *Philos. Mag.* **21**, 225 (1911).
- ⁶J. C. Toussaint *et al.*, Report DJC-SEPAGE-LMJ-20000-RXP-CDD-MOS 17982/A (2014).
- ⁷T. Bonnet *et al.*, *Rev. Sci. Instrum.* **84**, 013508 (2013).
- ⁸J.-P. Nègre, Report CEA-R-6271, ISSN: 0429-3460, 2011.
- ⁹K. A. Tanaka *et al.*, *Rev. Sci. Instrum.* **76**, 013507 (2005).
- ¹⁰N. Nakanii *et al.*, *Rev. Sci. Instrum.* **79**, 066102 (2008).
- ¹¹H. Chen *et al.*, *Rev. Sci. Instrum.* **79**, 033301 (2008).
- ¹²T. Bonnet *et al.*, *Rev. Sci. Instrum.* **84**, 103510 (2013).
- ¹³G. Boutoux, N. Rabhi *et al.*, *Rev. Sci. Instrum.* **86**, 113304 (2015).
- ¹⁴E. d’Humières *et al.*, “Modelling of high energy particles and radiation production in the PETAL experiments,” Nuclear Fusion (submitted).
- ¹⁵S. Corde *et al.*, “Femtosecond x-rays from laser-plasma accelerators,” *Rev. Mod. Phys.* **85**, 1 (2013).
- ¹⁶S. Agostinelli *et al.*, *Nucl. Instrum. Methods Phys. Res., Sect. A* **506**, 250 (2003).
- ¹⁷Y. Glinec *et al.*, *Rev. Sci. Instrum.* **77**, 103301 (2006).
- ¹⁸G. E. Giakoumakis and D. M. Miliotis, *Phys. Med. Biol.* **30**, 21 (1985).
- ¹⁹J. Belloni, H. Monard, F. Gobert, J. Larbre, A. Demarque, V. De Waele, I. Lampre, J. Marignier, M. Mostafavi, J. Bourdon *et al.*, *Nucl. Instrum. Methods Phys. Res., Sect. A* **539**, 527 (2005).
- ²⁰A. Buck *et al.*, *Rev. Sci. Instrum.* **81**, 033301 (2010).
- ²¹B. Hidding *et al.*, *Rev. Sci. Instrum.* **78**, 083301 (2007).